Materials Today Bio 16 (2022) 100359

Contents lists available at ScienceDirect

Materials Today Bio

journal homepage: www.journals.elsevier.com/materials-today-bio

Biomimetic macrophage membrane-coated gold-quantum dots with tumor microenvironment stimuli-responsive capability for tumor theranostic

Fan Wang [a,1], Qinghua Yu [a,1], Jia Li [a,1], Junhao Jiang [b], Tao Deng [a,**], Chao Yu [a,c,*]

[a] Research Center of Pharmaceutical Preparations and Nanomedicine, College of Pharmacy, Chongqing Medical University, Chongqing, 40016, China
[b] Chongqing Key Laboratory for Pharmaceutical Metabolism Research, College of Pharmacy, Chongqing Medical University, Chongqing, 40016, China
[c] Chongqing Pharmacodynamic Evaluation Engineering Technology Research Center, College of Pharmacy, Chongqing Medical University, Chongqing, 40016, China

ARTICLE INFO

Keywords:
Carbon dots
Gold nanoparticle
Inter-particle assembly
Tumor microenvironment
Theranostic

ABSTRACT

Tumor microenvironment (TME) is intently related to tumor growth, progression and invasion, leading to drug resistance and insufficient therapeutic efficacy. However, remodeling TME and utilizing TME for exploring intelligent nanomaterials that can realize tumor theranostic is still challenging. Nowadays, the theranostic based on chemotherapy exposes some deficiencies, such as low targeting, weak permeability and premature clearance. Furthermore, it is challenging to cure drug-resistant tumors effectively. For the sake of solving these problems, a biomimetic decomposable nano-theranostic (MMV-Au-CDs-DOX) was well-established in this work. The Au-CDs are coated with macrophage-derived microvesicle to realize drug release accurately and enhance the biocompatibility of internal nanoparticles. Furthermore, MMV-Au-CDs-DOX would locate in the inflammation position of tumor, and disintegrate correspondingly into pieces with certain different functions stimulated by TME. Subsequently, the released anti-tumor nanodrugs were used for multimodal therapy, including chemotherapy and hemodynamic therapy. In addition, combined with the ability of Au-CDs to recognize GSH specifically, the off-on fluorescent probe was constructed to monitor the GSH of tumor cells and provided information on chemotherapy resistance.

Credit author statement

Fan Wang, Qinghua Yu and Jia Li: Methodology, Investigation, Writing – original draft. **Junhao Jiang:** Methodology, Investigation. **Tao Deng and Chao Yu:** Conceptualization, Supervision, Writing – review & editing.

1. Introduction

Tumor microenvironment (TME), presenting hypoxia, reducing conditions, acidic pH and hydrogen peroxide (H_2O_2) overexpression characteristics and so on [1], produce a breeding ground for carcinoma cells origination and residence, which could induce malignant tumor progression, high drug resistance and aggressive metastasis [2,3], and pose a severe challenge for the development of novel anticancer strategies. However, from another perspective, the TME distinct from normal cells and tissues provides effective therapeutic targets for cancer treatment [4]. To achieve precise treatment of tumor, the adoption of intelligent nanomaterials that exhibit TME stimuli-responsive theranostic capacities has been expected to be one of the ideal ways to improve therapeutic efficiency while minimizing side effects [5]. Although broad researches have been conducted on the development and construction of the TME-triggered theranostic platform, endowing such a system with satisfactory characteristics of programmed control is still highly desirable [6–8].

Assisting by the fast development of nanotechnology, engineered nanomaterials have become an ideal way to construct a programmed control system under the extracellular and intracellular TME activation [9–11]. Among them, the procedural disintegration of nanocomposites is a valuable method for producing size-tunable nanomaterials. Generally,

* Corresponding author. Research Center of Pharmaceutical Preparations and Nanomedicine, College of Pharmacy, Chongqing Medical University, Chongqing, 40016, China.
** Corresponding author. Chongqing pharmacodynamic evaluation engineering technology research center, College of Pharmacy, Chongqing Medical University, Chongqing, 40016, China.
E-mail addresses: 190444@cqmu.edu.cn (T. Deng), yuchao@cqmu.edu.cn (C. Yu).
[1] These authors contributed equally to this work.

https://doi.org/10.1016/j.mtbio.2022.100359
Received 16 May 2022; Received in revised form 6 July 2022; Accepted 8 July 2022
Available online 12 July 2022

the hierarchical self-assembly of complex nanocomposites is the prerequisite for achieving procedural decomposition. Meantime, the process of self-assembly is mediated by structurally different building blocks organic macromolecules between inorganic nanoparticles using synergetic non-covalent interactions, such as electrostatic interactions, hydrophobic interactions and hydrogen bond interactions [12,13]. Of note, the excellent availability of building block units, the simplicity of synthesis and synergistic emerging properties make self-assembly work as a powerful technique for constructing functional hierarchical materials [14,15]. More importantly, on the concept of theranostic, fabricating nanomaterials using assembly strategies by integrating with diverse inorganic nanoparticles could also endow nanomaterials with multifunction besides improved enhanced-permeation-and-retention (EPR) effect, including drug loading, magnetic, heating, and fluorescence effects; while efficient self-assembly might be used to control the size, surface charge, and water-solubility of the nanocomposites, and resulting in new applications, ranging from optical and electronic devices to cellular imaging, biological sensing and disease treatment [16–18].

Carbon dots (CDs) and gold nanoparticles (AuNPs), the versatile and functional materials, usually served as the "star" building block units, gained increasing interest due to their extensive application to delivery or act as the theranostic agent to lesion location, especially for tumor [19,20]. Basically, CDs is a potential fluorescence carbon-based material with uniform size, remarkable modifiability and biocompatibility [21,22]. However, the size of traditional CDs is usually less than 10 nm which restrict its accumulation on the tumor site effectively because of the poor effect of EPR, leading to reduced theranostic outcomes [23,24]. Furthermore, the uncontrolled size and miscellaneous surface ligands are double-edged, limiting the flexibility of application, while provided multiply dentate N/O donor atoms contained ligands for integrating metal nanoparticles. Meantime, the non-therapeutic of CDs restricted its application in drug therapy [25]. As AuNPs were widely used for tumor photothermal therapy, the catalytic activity, such as dynamic therapy, was rarely investigated [26]. Interestingly, AuNPs could be successfully dispersed on the carbon-based substrate, and the catalytic activities of the nanomaterials were appropriately applied by controlling their nanostructures and compositions [27,28]. What's more, electron transfer between CDs and AuNPs would induce the dynamic change of fluorescence during assembling, which is a benefit for constructing the off-on sensing interfaces.

Herein, in this paper, we fabricated an intelligent nanomaterial, called Au-CDs, via "step by step" inter-particle assembled, which exhibited glutathione (GSH) and H_2O_2 sensitive procedural disintegration and fluorescence enhancement, besides size controllability and variability, and be used as the specific anti-tumor adjuvants after being biomimetic modified by macrophage-derived micro-vesicle (MMV) for the treatment of the lung metastatic breast cancer, as well as for the test of tumor drug resistance. The biomimetic MMV-Au-CDs-DOX nanocomposite would locate in the inflammation position of tumor driven by the chemotactic cell membrane and disintegrate correspondingly into pieces with certain different functions stimulated by TME, such as GSH and H_2O_2, which exhibited selective tumor targeting and precisely controlled drug release. Subsequently, the released anti-tumor nanodrugs were used for multimodal tumor therapy, including chemotherapy (DOX) and hemodynamic therapy. In addition, combined with the ability of Au-CDs to recognize GSH specifically, the off-on fluorescent probe was constructed to monitor the GSH in the tumor lesion of cancer patients and provide the information on chemotherapy resistance (as shown in Scheme 1).

2. Materials and methods

2.1. Materials

Cetylpyridinium chloride monohydrate (CPC, 98%), sodium hydroxide (NaOH, 97%), gold chloride hydrate ($HAuCl_4$, 45.5%), sodium borohydride ($NaBH_4$, 98%), 3-(4,5-dimethylthiazol-2-yl)-2,5-diphenyltetrazolium bromide (MTT), hydrochloric acid (HCl, 37%), dichloromethane (DCM, 99.9%) were purchased from Shanghai Aladdin Bio-Chem Technology Co., Ltd.

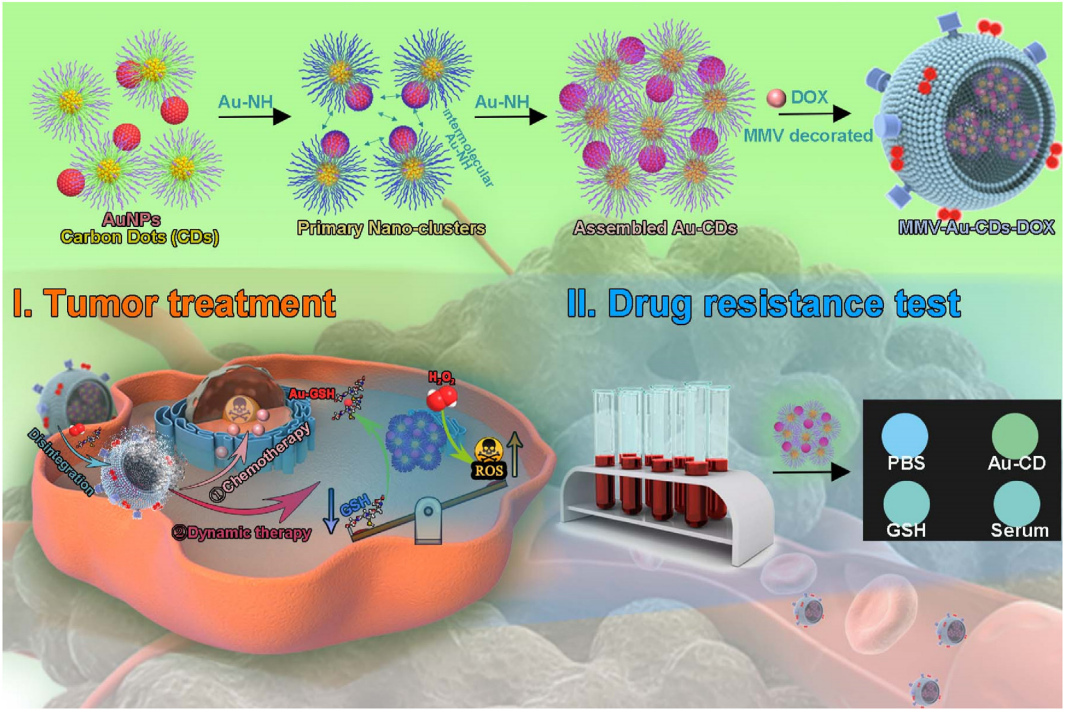

Scheme 1. Overall synthetic schemes for MMV-Au-CDs-DOX nanocomposite via "step by step" inter-particle assemble strategies, as well as their following bio-applications.

The human umbilical vein endothelial cells (HUVEC) and murine breast cancer 4T1 cell line (4T1 cells) were obtained from Type Culture Collection of the Chinese Academy of Sciences (Shanghai, China). Healthy male ICR mice (18–20 g) were purchased from Laboratory Animal Center, Chongqing Medical University, Chongqing, China.

All the animal procedures in this work were performed in accordance with the Guidelines for Care and Use of Laboratory Animals of Chongqing Medical University, and approved by the Animal Ethics Committee of Chongqing Medical University (SCXK2018-0003).

2.2. Apparatus

UV–Vis absorption spectra were recorded with a Model Ultra-6600A (Rigol, China). PL spectra were recorded by RF-5301 spectrofluorophotometer (Shimadzu, Japan). All optical measurements were performed at room temperature. The size and ζ-potentials measurements of Au-CDs-based nanocomposites were characterized by Mastersizer 2000 Laser Particle Size Analyzer (LPSA, Malvern, British). In addition, the TEM images of the samples were taken on a JEOL JEM-2100 transmission electron microscope with an acceleration voltage of 200 kV. Carbon coated copper grids were dipped in sample solution to deposit them on the film. The absorbance for the MTT assay was measured with a Tecan's Infinite M200 microplate reader at a wavelength of 490 nm. Finally, the fluorescence images of cells were obtained by confocal laser scanning system (Leica, Germany).

2.3. Synthesis of cpc-CDs cluster

The water-soluble cpc-CDs cluster was prepared according to our previous reports [29]. In brief, 2.0 M NaOH was added into a CPC aqueous solution (15 mM) and left to stand at room temperature without applying any external energy. The color of the mixture solution turned from colorless to light yellow and then to wine red as the reaction time proceeded, indicating the carbonisation of CPC. The reaction was terminated 24 h later by adjusting to neutral (pH = 7) with HCl. After the reaction, oil-soluble CDs could be separated by adding DCM to extract the oil-soluble CDs into the bottom organic layer. Subsequently, the oil-soluble CDs were transferred into water by simply ultrasound assistant self-assembly. Typically, 50 μL of the oil-soluble CDs (1 mg/mL) in DCM were mixed with 1 mL water by sonication in a cold-water bath. The dichloromethane was gradually evaporated, yielding a slightly turbid solution. After centrifugation, the aqueous CDs-clusters were obtained and kept at room temperature for further use.

2.4. Preparation of Au-CDs

Au-CDs was fabricated by the inter-particle assembly of gold nanoparticles and cpc-CDs. Firstly, 200 μL of the cpc-CDs were mixed in 1.9 mL NaOH solution (pH = 8.0). Subsequently, 1% $HAuCl_4$ solution (300 μL) dropped slowly into the above reaction solution with slightly stirring at 30 °C. Dripping finished, a little superfluous $NaBH_4$ solution (1 mg/mL) was slowly added into the reaction system until the color of the mixture solution turned from light yellow to dark grey. Then, the obtained aqueous solution was further centrifuged at 5000 rpm for 10 min, separated the supernatant to obtain light brown Au-CDs aqueous solution, which was changed into solid grey powder after freeze-drying.

2.5. Drug loading

To construct Au-CDs-DOX and Au-CDs-ICG, 1 mg DOX or 1 mg ICG was first dissolved in dichloromethane (1 mL) and then added into 4 mL prepared Au-CDs solution under sonication in a cold-water bath. After the dichloromethane was evaporated, the limpid Au-CDs-DOX or Au-CDs-ICG nanoparticles were yielded in a water solution. Followed by stirring at room temperature for 24 h, the crude product was purification by dialysis (MWCO 1000 D) in distilled water for another 24 h. Furthermore, the standard curve of DOX was settled by the UV absorption peak (λ = 550 nm) to calculate the concentration of DOX in Au-CDs-DOX.

2.6. Preparation and characterization of MMV-Au-CDs-DOX

The MMV was prepared according to our previous work [30]. Then, MMV was added to the Au-CDs-DOX solution at a protein ratio of 1:10 (w/w, protein to Au-CDs) and sonicated for 5 min at a power of 100 W to collect crude MMV-Au-CDs-DOX. The free MMV was removed by centrifugation at 4000 rpm for 20 min. After centrifuging at 15,000 g for another 30 min, the purified MMV-Au-CDs-DOX was collected and lysed for western blot and SDS-PAGE electrophoresis analysis (total macrophages were used as a control for analysis).

2.6.1. Drug release

To investigate the DOX release behavior under different condition, 1 mL of each formulation encapsulated 0.7996 mg DOX was conveyed into a dialysis bag (MWCO 1000 D) and then put in 10 mL PBS with the simulated TME condition (pH = 5, GSH = 10 mM) or the neutral condition (pH = 7). Finally, 1 mL release medium was collected at predetermined time points, followed by replenishing with an equal volume of fresh medium, and the UV–vis absorption quantified the released DOX.

2.6.2. In vitro and in vivo GSH detection

To examine whether the synthesized Au-CDs have the potential ability to detect endogenous and exogenous GSH, firstly, 100 μL GSH (10 mM) was added into 1 mL Au-CDs solution under different pH (5, 8 and 12), and the UV–vis collected the absorption change. Next, 100 μL GSH (10 mM) was added into 1 mL Au-CDs solution (pH = 8) in different incubation times (0, 5, 10, 20 and 30 min, respectively), and UV–vis also observed the absorption change. Furthermore, the GSH sensing sensitivity of Au-CDs was evaluated by range concentration detection. In brief, different concentrations of GSH (0–40 mM) were added into 1 mL Au-CDs solution for incubating 5 min followed by UV irradiation. Digital photos took the properties change of solution. Finally, we examined the intracellular GSH detection ability of Au-CDs, 10 mM GSH was added into the prepared 4T1 cells in 12-well plates, after incubating 30 min, the Au-CDs was added and incubated for another 90 min, followed by washing with sterilization PBS, CLSM acquired the fluorescence image of intracellular GSH.

2.7. In vitro cell study

Cell Culture: The cells (4T1 and HUVEC) were cultured in DMEM medium supplemented with 10% (v/v) calf serum, penicillin (100 U/mL) and streptomycin (100 mg/mL) at 37 °C in a humidified atmosphere containing 5% CO_2.

Cytotoxicity Evaluation: The *in vitro* cytotoxicity of nanocomposites was assessed preliminarily by the colorimetric MTT assay using 4T1 and HUVEC cell lines. Typically, the cells were seeded onto 96-well plates (1×10^4 cells per well) and cultured at 37 °C in a humidified incubator with 5% CO_2 for 24 h. Then, the cells were incubated with sample solutions at a wide concentration range from 10 μg/mL to 300 μg/mL for another 24 h at 37 °C. The cells were rinsed using fresh DMEM medium, followed by incubation with 20% MTT (10 μL) at 37 °C for 4 h. After the medium was discarded, DMSO (150 μL) was used to lyse the cells. The microplate reader recorded the absorbance at 570 nm. Every experiment was conducted quintic, and the cell viability was calculated by referring to the control group without the sample treatment.

In Vitro Cell Imaging: The cell imaging experiments were performed with 4T1 cells. In brief, these cells were seeded in laser confocal scanning microscope (LCSM) culture dishes were incubated at 37 °C in a humidified incubator with 5% CO_2 until the whole cells occupied about 70% of the dish bottom space. Subsequently, Au-CDs-based nanocomposites DMEM solution (200 μL) was added to cells for co-incubation 2 h to stain. Before being imaged by LSCM, the cells were co-incubated with Hoechst

33,342 for another 30 min to stain the nucleus. Then, the cells were washed by fresh DMEM three times, and the samples were measured under laser light (λ = 405, 488 nm) excitation.

2.8. In vivo study

Establishment of 4T1 breast cancer lung metastasis model: Tumor migration models were built up by tail vein injection of 4T1 cells (obtained from the mouse cancerous ascites) into each ICR mouse (4–6 weeks old, 18–20 g). After growing for 2 weeks, all of the mice were sacrificed to evaluate the area of necrotic tissues on the lung surface.

In Vivo Fluorescence Imaging: Normal saline injection (200 μL) containing Au-CDs-based nanocomposites (100 μg) was injected into the 4T1 lung metastasis mice (n ≥ 3) through the vena caudalis. Then, the mice were imaged at predetermined time intervals (0–72 h) post-injection with a homemade *in vivo* small animal NIR imaging system, and the background image was taken before injection.

2.9. Histology examination

Histology analysis was carried out on the 15th day after the treatment. Typical heart, liver, spleen, lung, kidney and tumor tissues of the mice in the control and best treatment groups were isolated. Then, the organs were dehydrated using buffered formalin, ethanol with different concentrations, and xylene. After that, they were embedded in liquid paraffin. The sliced organs and tumor tissues (3–5 mm) were stained with hematoxylin and eosin (H&E) and examined by a microscope.

3. Results and discussion

3.1. Fabrication of the "off-on" fluorescent Au-CDs

Well-designed procedural-disintegrated nanomaterials were an effective way to fulfil nanocomposite with specific deformation to adapt to the complex tumor microenvironment for effective targeting and permeability. However, poor functionality and non-monitoring greatly limited its bio-application. Herein, a promising "off-on" fluorescent procedural-disintegrated nanomaterials with the therapeutic function was designed due to carbon dots -supported gold.

As shown in Fig. 1A, the conception is based on the fact that (i) cpc-CDs was a potential imaging-guided drug carrier with excellent self-assembly performance discovered by our team, which could self-regulate size by adjusting amphiphilic precursor. In addition, the widespread N/O donor dentate atoms on the surface also provided the binding sites for AuNPs, while the weaker Au–N bond would disintegrate and rebind into Au–S once encountered GSH for realizing the construction and disintegration of Au-CDs comprehensively, and the release of the upload cargo in fixed space and time. (ii) Individual Au atoms or small Au clusters on the carbon-based substrate could catalyze H_2O_2 into ROS for inducing the process of tumor apoptosis. (iii) electron transfer between cpc-CDs and AuNPs went through the whole process of assembling and dissociation, even catalysis, which achieved the "off-on" fluorescence.

Compared with the initial cpc-CDs, the absorption spectrum (Fig. S1) of as-prepared Au-CDs emerged at a novel peak around 500 nm, which belonged to AuNPs, indicating the successful upload of AuNPs. Interestingly, during the assembling between cpc-CDs and AuNPs, the bright

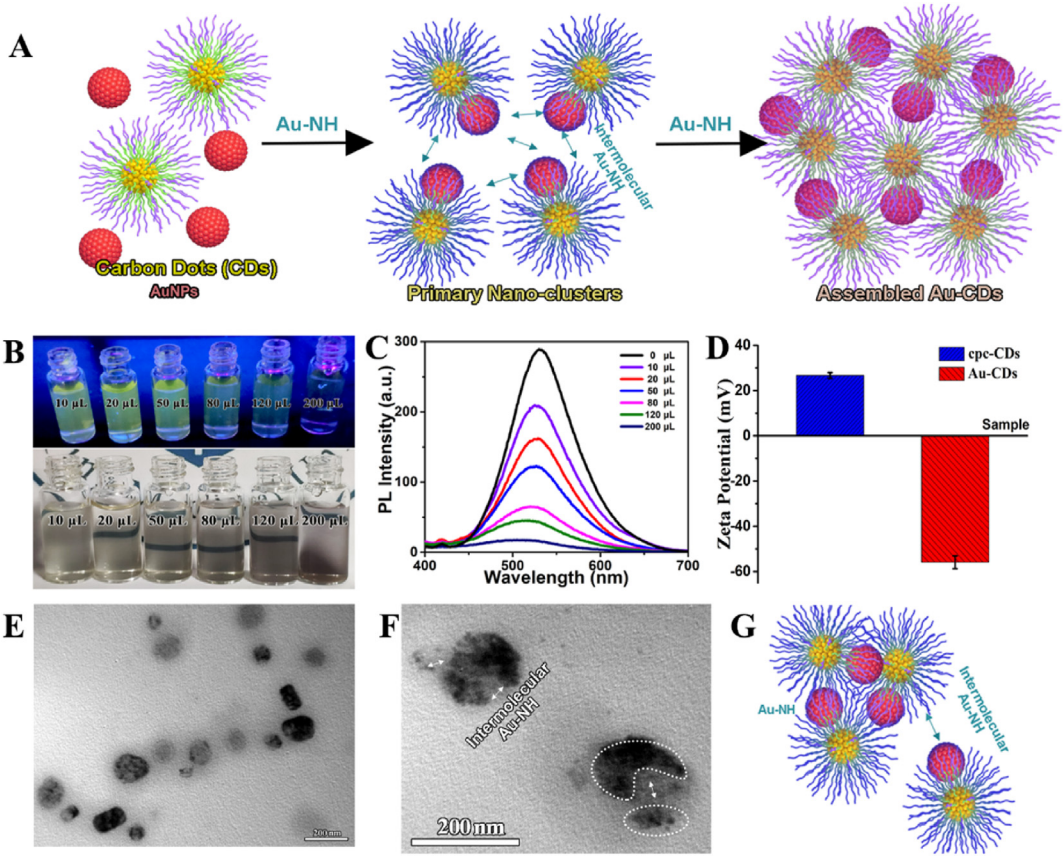

Fig. 1. Preparation and characterization of Au-CDs. (A) Schematic illustration of Au-CDs preparation. (B) The true-color photographs of as-prepared Au-CDs captured under room light and UV light (λ_{max} = 365 nm) excitation. (C) PL spectra (λex = 365 nm) of different concentrations of Au mediated carbon dots nanocomposites. (D) ζ-Potential variation trend of cpc-CDs-AuNPs during assemble. (E) The TEM image of the intermediate assembled state. Scale bar = 200 nm. (F) The morphology of Au-CDs. Scale bar = 200 nm. (G) Cartoon model of the self-assembled procedure of Au-CDs. (For interpretation of the references to colour in this figure legend, the reader is referred to the Web version of this article.)

yellow fluorescence of cpc-CDs was disappeared gradually with the increase of HAuCl4 concentration (Fig. 1B). And the photoluminescence (PL) spectra (Fig. 1C) intuitively exhibited the process of fluorescent quenching accompanied by adding HAuCl4 solution. As expected, the size of the assembled cpc-CDs-AuNPs was also depended on the concentration of HAuCl4 (Fig. S2). This phenomenon could be attributed to the intermolecular or intramolecular Au–NH bond (Fig. 1G). We also observed, during the process of assembling, the ζ-potential of the complex in PBS overturned from 28 mV (cpc-CDs) to −58 mV (Au-CDs) (Fig. 1D), indicating the assembled nanocomposite was stable in the dispersion medium. More importantly, at the intermediate assembled state, the morphology of the as-prepared composite was trending to aggregate (Fig. 1E). Essentially, the driving force of aggregation was inter/intra-molecular interactions. As cpc-CDs and AuNPs constructed Au-CDs, Au–NH bond was rife with the surface of cpc-CDs and the early (or smaller) assembled cpc-CDs-AuNPs, as well as the whole process of formation. And subsequently, Au-CDs were assembled into the spherical complexes, of which the diameter was ~200 nm (Fig. 1F). The result of dynamic light scattering (DLS) further showed (Fig. S3) that the size of Au-CDs is around at 192 nm. Furthermore, element EDS (Fig. S4) and mapping analysis (Fig. S5) results of Au-CDs manifested the existence of carbon, nitrogen oxygen and gold element. Above results illustrated the successful synthesis of Au-CDs. In addition, the stability experiments of Au-CDs were carried out (Fig. S6). We completed the UV–vis absorption of Au-CDs after dispersed in ultrapure water, PBS, and cell culture medium (DMEM/F-12 with 10%FBS) for 24 h. The photographs were taken under white light or 365 nm laser irradiation before and after placement for 24 h, respectively. The results showed that Au-CDs were stable in each solution, and no significant agglomeration occurred. Interestingly, weak fluorescence appears when Au-CDs were dispersed in DMEM/F-12, inspiring we further investigated the DMEM/F-12 alone. Fig. S7 display that the DMEM/F-12 without containing Au-CDs had the intense fluorescence, which could explain the weak fluorescence of Au-CDs when DMEM/F-12 was used as dispersion medium.

3.2. Disintegration and mimetic enzyme properties of Au-CDs

As the weak Au–NH binding force among AuNPs and cpc-CDs tended to fracture or be replaced by stronger chemical bonds (e.g. Au–S bond), which caused the disintegration of the system eventually [31,32]. As we know, the rich complexity of the TME is now recognized not only as an integral factor contributing to carcinogenesis but also as playing critical roles modulating cancer therapy, and the mild acid TME with the high level of H_2O_2 and GSH was most recognized by researchers. Herein, the different morphologies of Au-CDs were captured by TEM before and after incubation with the simulated TME (Fig. 2B–D).

Essentially, the fracture or formation of chemical bonds belonged to electron transfer, and the surface electron flow further affected the catalysis of metal nanoparticles, especially for AuNPs [33,34]. Then we discovered that the different appearance of Au-CDs had a certain influence on the fluorescence and peroxidase property by studying PL and catalytic activity of Au-CDs before and after incubation with GSH and H_2O_2, which was the similar physiological concentration with TME. As shown in Fig. 2E, the change of emission intensity was reversible after mixing with H_2O_2. During the initial 20 min incubating, the fluorescence of Au-CDs was restored gradually, and the rate of PL increase was most significant in the early stage. Accompanied with decreasing in increment, even reversal (30–60 min), the fluorescence intensity of Au-CDs reduced

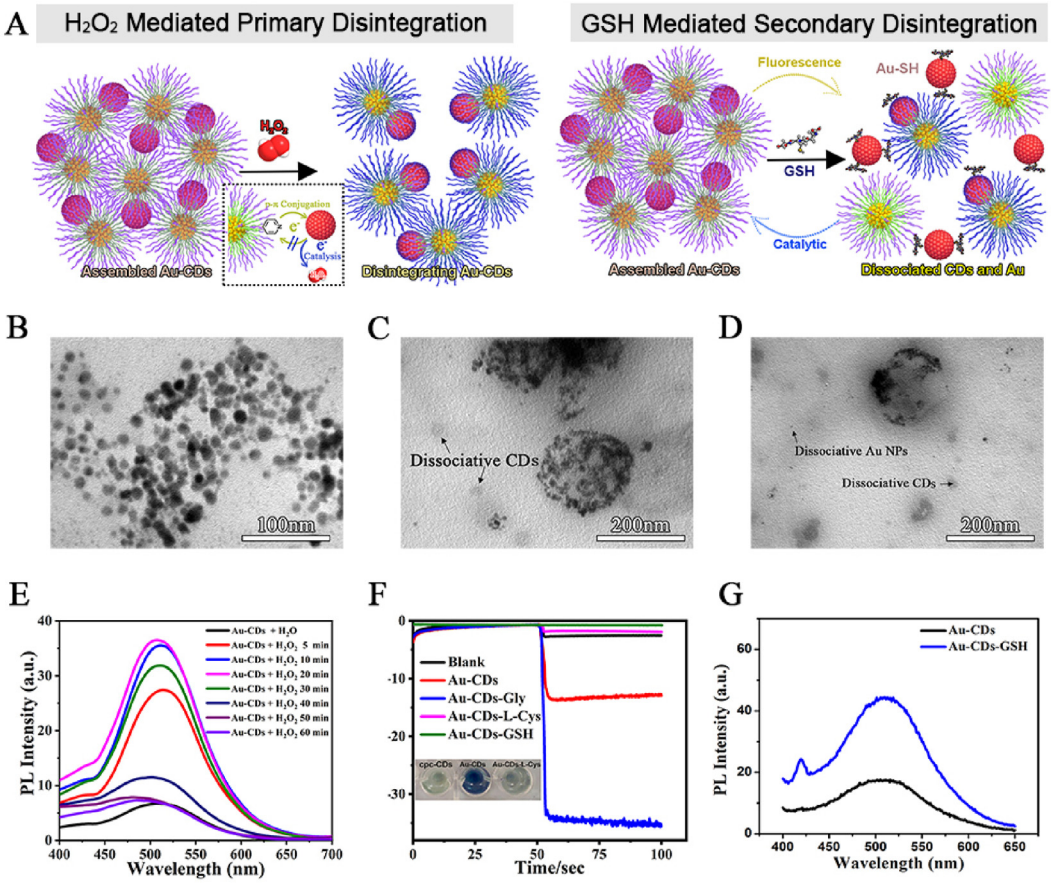

Fig. 2. *In vitro* stimuli-responsiveness of Au-CDs to GSH and H_2O_2. (A) Schematic diagram of Au-CDs disintegrated by H_2O_2 and GSH. TEM image of (B) integral Au-CDs and dis-assemble by (C) H_2O_2 and (D) GSH. (E) PL spectra of Au-CDs during co-incubation with H_2O_2. (F) i-t curve of Au-CDs modified electrodes in PBS solution containing Gly (Glycine), L-Cys (L-Cysteine) and GSH. (G) PL spectra of Au-CDs during co-incubation with GSH.

to the origin. Alternately, this phenomenon could also be explained by the electron flowing as reductive AuNPs catalyzing H_2O_2, causing the disintegration and reorganization of the Au–NH bond. At the beginning of the reaction, the weak Au–NH bond between cpc-CDs and AuNPs was destroyed by the electron flux, and the fluorescence was restored. With the response and consumption of H_2O_2, Au-CDs disintegrated into a smaller spherical particle (~12 nm, Fig. 2C) compared with the integral Au-CDs (Fig. 2B). As Au–S bonds are more potent than Au–N bonds, the assembled Au-CDs would completely dissociate when they coexist with sulfur compounds, like GSH and cysteine, which was proved by TEM (Fig. 2D). Fig. 2C and D showed the morphologies of Au-CDs after reacting with H_2O_2 and GSH, respectively, appeared with three existing forms of disaggregation, included incompletely dissociated Au-CDs (the agglomerates with voids) and dissociative cpc-CDs (low contrast ~ 10 nm particle) and AuNPs (the darker ~2 nm nanodot). The alterations of fluorescence intensity (Fig. 2G) and oxidase activity (Fig. 2F) were further verified above conjecture. The fluorescence was irreversibly and permanently illuminated after AuNPs were stripped. The peroxidase property weakened due to the more vital binding ability to surface electrons of new Au–S bonds and the larger size of gold nanoparticles.

3.3. In vitro detection of glutathione

Chemotherapy is the conventional approach to curing tumor diseases. However, tumor micro-environment is characterized by high glutathione (GSH) expression, which seriously limits its clinical application, especially for drug resistance of chemotherapeutic hydroquinone agents [35,36]. Research shows that glutathione content related with multidrug resistance-associated protein, even interfered with the efficacy of radiotherapy [37]. Grasping the concentration of GSH as soon as possible, simplicity and speed are necessary for patients to acquire a more reasonable medical plan. As mentioned above, Au-CDs disintegrated after incubation with the GSH (equivalent to the TME concentration), accompanied by the fluorescence emission resuming, which was similar to the "off-on sensor" extremely.

As shown in Fig. 3A, the "off-on" sensor test paper was obtained by dropping Au-CDs into polyvinylidene fluoride membrane (PVDF membrane, the self-fluorescence was lower than that of ordinary paper). In order to get the optimal detection conditions and inspection time, the solution containing Au-CDs was co-incubated with 10 mM GSH in different pH within a certain time range (Fig. 3B–E). As shown in Fig. 3B, the characteristic fluorescence emission of Au-CDs fluctuated within a narrow range under different pH conditions (the pH value was 5, 8 and 12), along with the slight fluorescence variation amplitude after reacting with GSH at pH 5 and 12. However, significantly, the fluorescence was obviously enhanced when pH was equal to 8. And the real sample photos (Fig. 3C) captured under the irradiation of ultraviolet lamp ($\lambda ex = 365$ nm) could visually reflect the different degrees of fluorescence increase. This phenomenon might be explained by the protonation of amino groups on the surface of Au-CDs. After that, the selection of optimum detection time was also performed in GSH solution (pH = 8). As shown in Fig. 3D, the fluorescence intensity of the original wholly quenched while Au-CDs rapidly enhanced, which could be visible to the naked eyes (Fig. 3E), during the first 5 min incubation, and with the stabilization of the enhanced trend, the time of maximum recovery of fluorescence was 30 min. Compared with these fluorescence enhancement values, the optimal co-incubation time was considered to be 5 min, which considerably shortened the detection time and cost.

In order to verify the sensing range for GSH, Au-CDs aqueous solution (pH = 8) was reacted with different concentrations of GSH for 5 min. Fig. 3F intuitively reflected the dynamic change of fluorescence during detection and displayed that with the increase of GSH concentration (from 0 to 40 mM). The amplitude of fluorescence recovery was gradually enhanced and could be directly photographed to record as long as the concentration increased to 10 mM (equivalent to the highest concentration of GSH in TME) [38]. Inspired by the sensitive GSH (an indicator of chemoresistance) response, Au-CDs was further developed as the guiding test paper for the clinical selection of tumor chemotherapy drugs. As shown in Fig. 3G, PVDF membrane-covered Au-CDs was imaged under the light and UV lamp, and it was apparent that the "Au-CDs + GSH" group exhibited the similar fluorescence as initial cpc-CDs, while showing a significant color difference compared with Au-CDs group (the blue PL emission in H_2O and CDs-AuNPs groups was the auto-fluorescence of background, and the more suitable paper will be selected for improvement in the future), which indicated Au-CDs infiltrative paper could be detected GSH *in vitro*. To further evaluate the ability to detect GSH in multi-level, 4T1 cell was selected as a model. Topically, an MTT assay was carried out before detecting intracellular glucose levels to assess the biocompatibility safety of Au-CDs (Fig. S8). As shown in Fig. 3H, the bright fluorescence of cpc-CDs was recovered as Au-CDs entered into cytoplasm fulling of glutathione. And the fluorescence is scattered outside 4T1 cell (white arrow in Fig. 3H) as the redundant GSH is added into the medium. The above results indicated that Au-CDs was an exciting material that acted as an "off-on" probe for glutathione detection in multi-level.

3.4. Drug loading, biomimetic construction and drug-sensitivity test of Au-CDs

Previous researches showed that cpc-based CDs was an ideal carrier for hydrophobic drugs, such as loading doxorubicin (DOX), owning to the inherent amphiphilicity of CPC, and the subsequent self-assembly and accompanying water transfer [39–41]. Furthermore, the secondary assembly of cpc-CDs mediated by AuNPs was beneficial for enhancing the EPR effect as the accurate size control of the resultant aqueous Au-CDs clusters. Accordingly, in this work, DOX was selected as the antitumor agent and was uploaded into the Au-CDs to fabricate the drug-loaded nanocomposites (Au-CDs-DOX) to study the subsequent tumor therapy and alleviate its side effects (Fig. 4).

To acquire the maximum upload volume, the oil-soluble DOX was prepared through a desalination reaction due to a previous study with a minor modification [43], and the obtained oil-soluble DOX was then mixed with Au-CDs to form co-assembled Au-CDs-DOX particles. As shown in Fig. 4A, Au-CDs-DOX contained the intrinsic UV–vis absorption of CDs, and characteristic absorption peaks of DOX (~495 nm) indicated the successful loading of DOX. Additionally, the following visible color change also manifested the practical construction. At 365 nm excitation, the fluorescence peak of DOX and cpc-CDs-AuNPs appear at 598 nm and 450 nm, and they both appear in the fluorescence spectra of Au-CDs-DOX (Fig. 4B), which further demonstrated the successful loaded of DOX. Additionally, drug loading (DL) efficiency was about 59.56% (Fig. S9).

Most studies have emphasized that the macrophages micro-vesicles (MMVs) derived from cells have the ability of organ- or cell-specific tropism, so it is likely to be an ideal natural drug carrier with low immunogenicity to enhance the targeting of the action site [30,42,44]. For the purpose of making Au-CDs-DOX turned into a higher targeted vehicle for tumor therapy not simply through passive targeting of EPR, we next impelled biomimetic construction by using the MMVs derived from Raw 264.7 after treating with cytochalasin B (a cell-permeable mycotoxin which can block the formation of contractile microfilaments, Fig. S10). TEM examinations defined the successful construction of MMV-Au-CDs-DOX as the presence of a transparent outer membranous structure around it (Fig. 4D), following the morphology of MMV (Fig. S11). To verify the correctness of formation, SDS-PAGE and western blot analysis experiments were performed to prove the existence of α4 and β1 integrin, which was the tumor-targeted ligands of macrophages, of the series of sub-unit of MMV-Au-CDs-DOX. Fig. 4E showed that MMV-Au-CDs-DOX had the same total protein expression spectrum as MMVs, extracted from the integral Raw 246.7 cells, while no protein signal was presented in the Au-CDs-DOX group. WB analysis (Fig. 4F) was further performed to prove the existence of α4 and β1 integrin. Regarded β-action signal as the control, α4 and β1 integrin (represent as Mac-1)

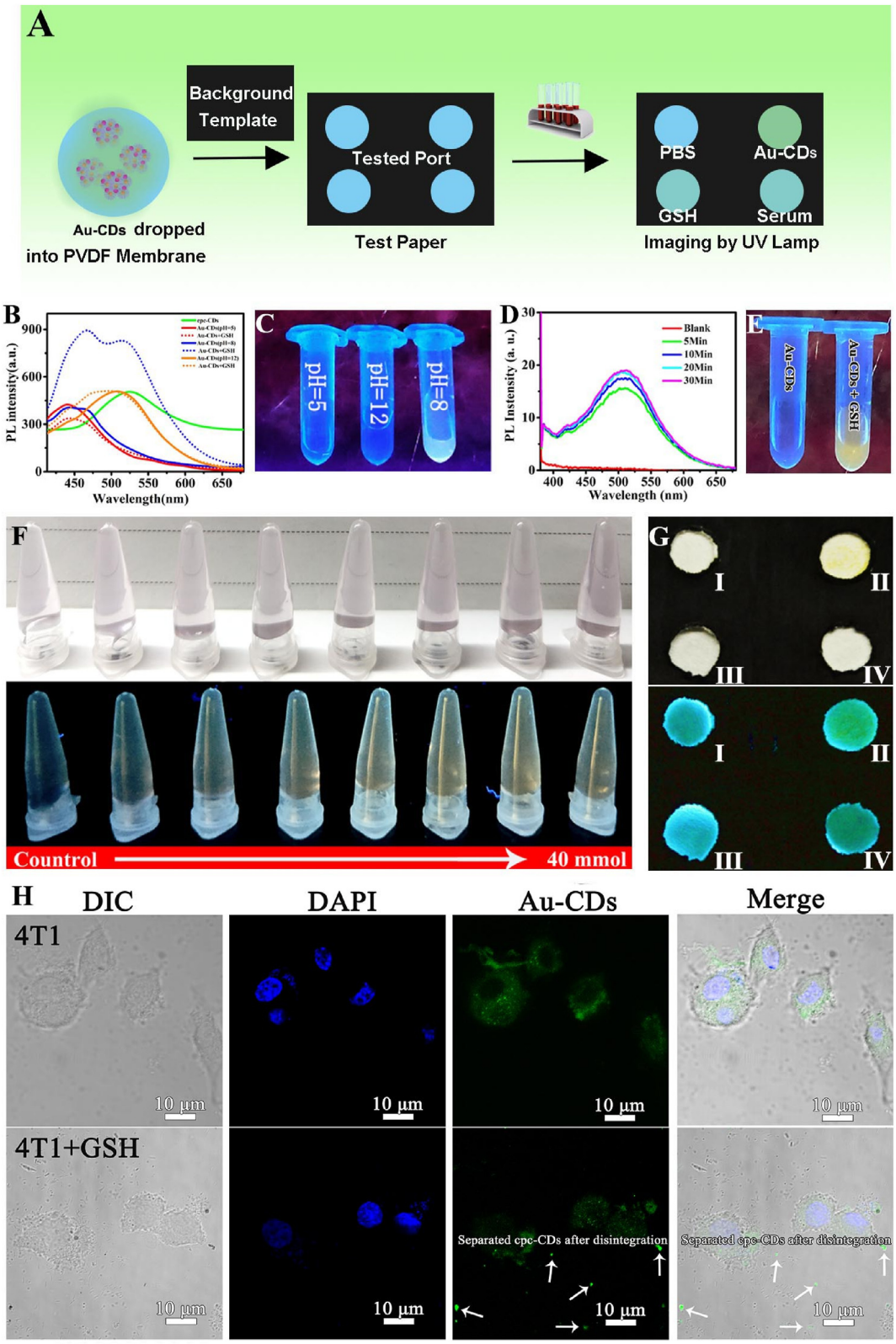

Fig. 3. Detection of GSH *in vitro*. (A) Schematic illustration of the construction and operation of GSH test paper. (B) PL spectrum and (C) Digital photo of Au-CDs excited under 365 nm laser during co-incubation with GSH in various pH. (D) PL spectrum and (E) Digital photo at different times of Au-CDs excited under 365 nm laser during 30 min co-incubation. (F) The true-color images of Au-CDs solution with a range concentration of GSH under room light (up) and UV lamp (down) with excitation wavelength at 365 nm. (G) Test paper reaction with or without GSH under room light (up) and UV lamp (down) with excitation wavelength at 365 nm (I: H_2O, II: cpc-CDs, III: Au-CDs, IV: Au-CDs + GSH). (H) CLSM image of intracellular GSH levels using Au-CDs probe. (For interpretation of the references to colour in this figure legend, the reader is referred to the Web version of this article.)

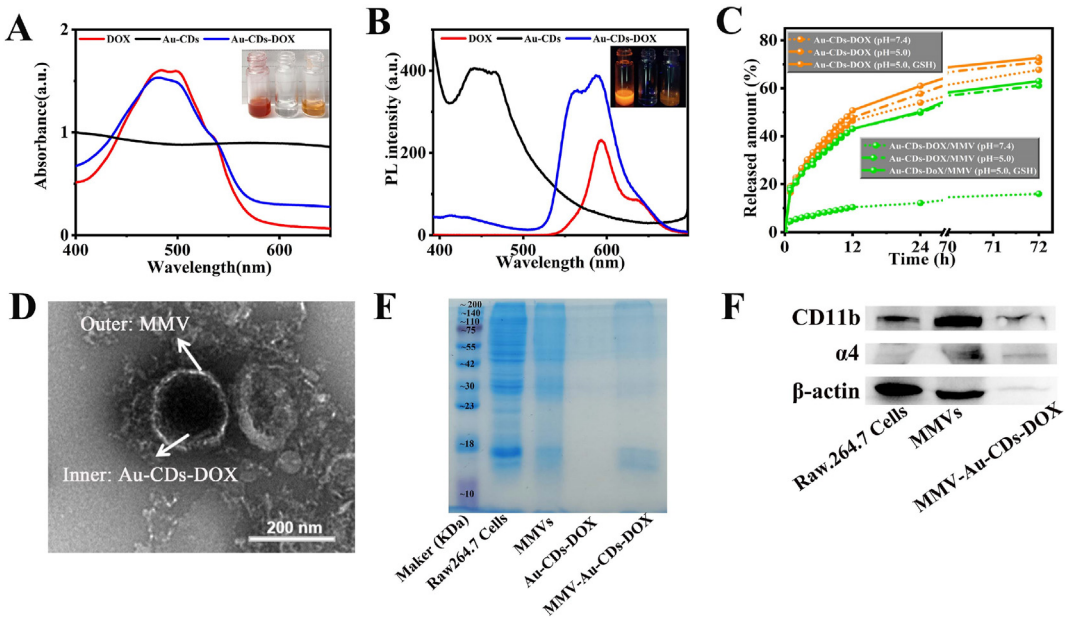

Fig. 4. The construction and characterization of MMV-Au-CDs-DOX. (A) Absorbance and (B) PL spectra of Au-CDs before and after DOX uploading, and the inserts were the digital photo of these samples captured under room light and 365 nm laser. (C) The curve of DOX release from Au-CDs-DOX and MMV-Au-CDs-DOX in different body fluid simulation, such as the fluid in peritumor tissue and blood. (D) TEM images of MMV-Au-CDs-DOX. The images of (E) SDS-PAGE and (F) western blot of Raw 264.7 cell, macrophages micro-vesicles and MMV-Au-CDs-DOX.

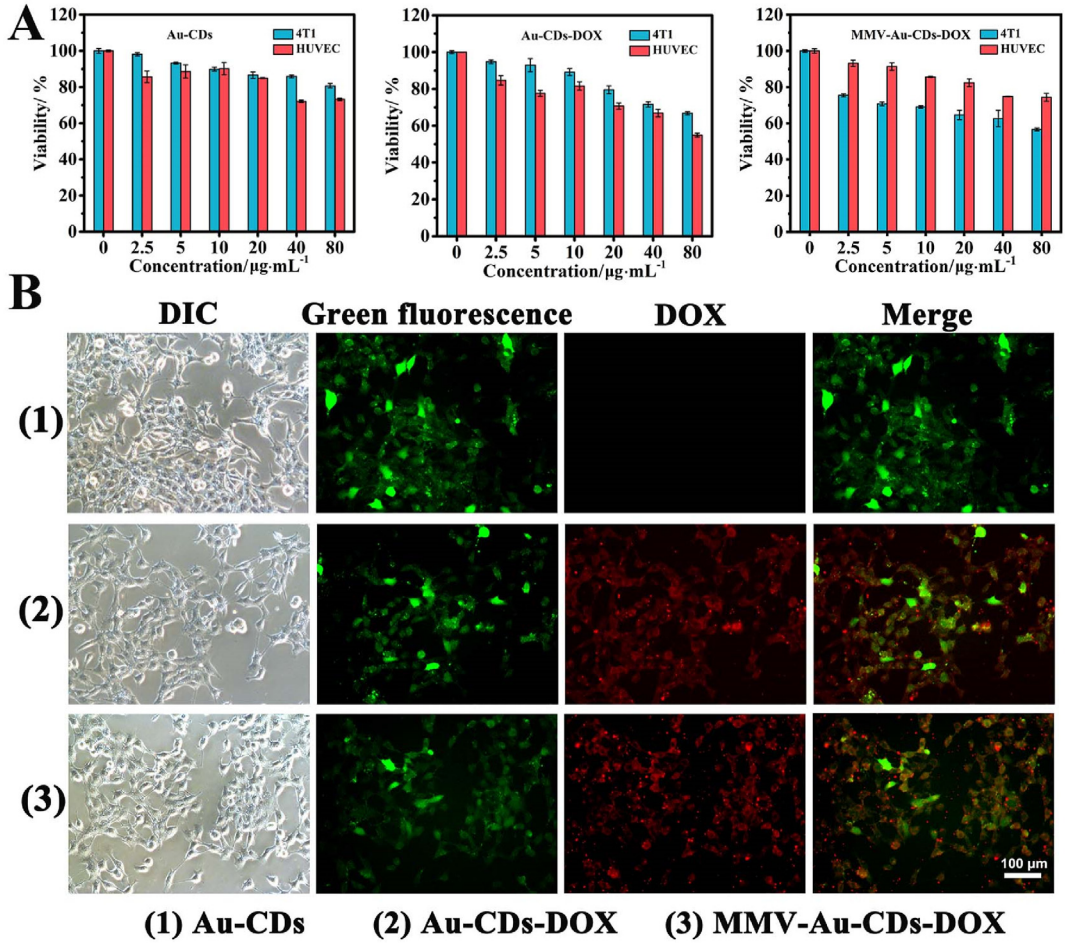

Fig. 5. Evaluation of the intracellular DOX release from MMV-Au-CDs-DOX using 4T1 cells. (A) Drug targeting experiment of MMV-Au-CDs-DOX via MTT assay (Concentration of different nanocomposites). (B) CLSM image of the intracellular DOX release in 4T1 cells incubated with DOX, Au-CDs and MMV-Au-CDs-DOX.

signal appeared in macrophage, MMV and MMV-Au-CDs-DOX group, while no protein signal was presented in the Au-CDs-DOX group. The above result showed that most of α4 and β1 integrins have remained after the micro-vesicles was separated and isolated from Raw 264.7 cell lines and cloaked drug carriers. After extruded by polycarbonate film, the average hydrated particle size of the obtained MMV-Au-CDs-DOX was about 180 nm, and its zeta potential was found to be −49.12 mV while Au-CDs-DOX was −53.67 (Fig. S12).

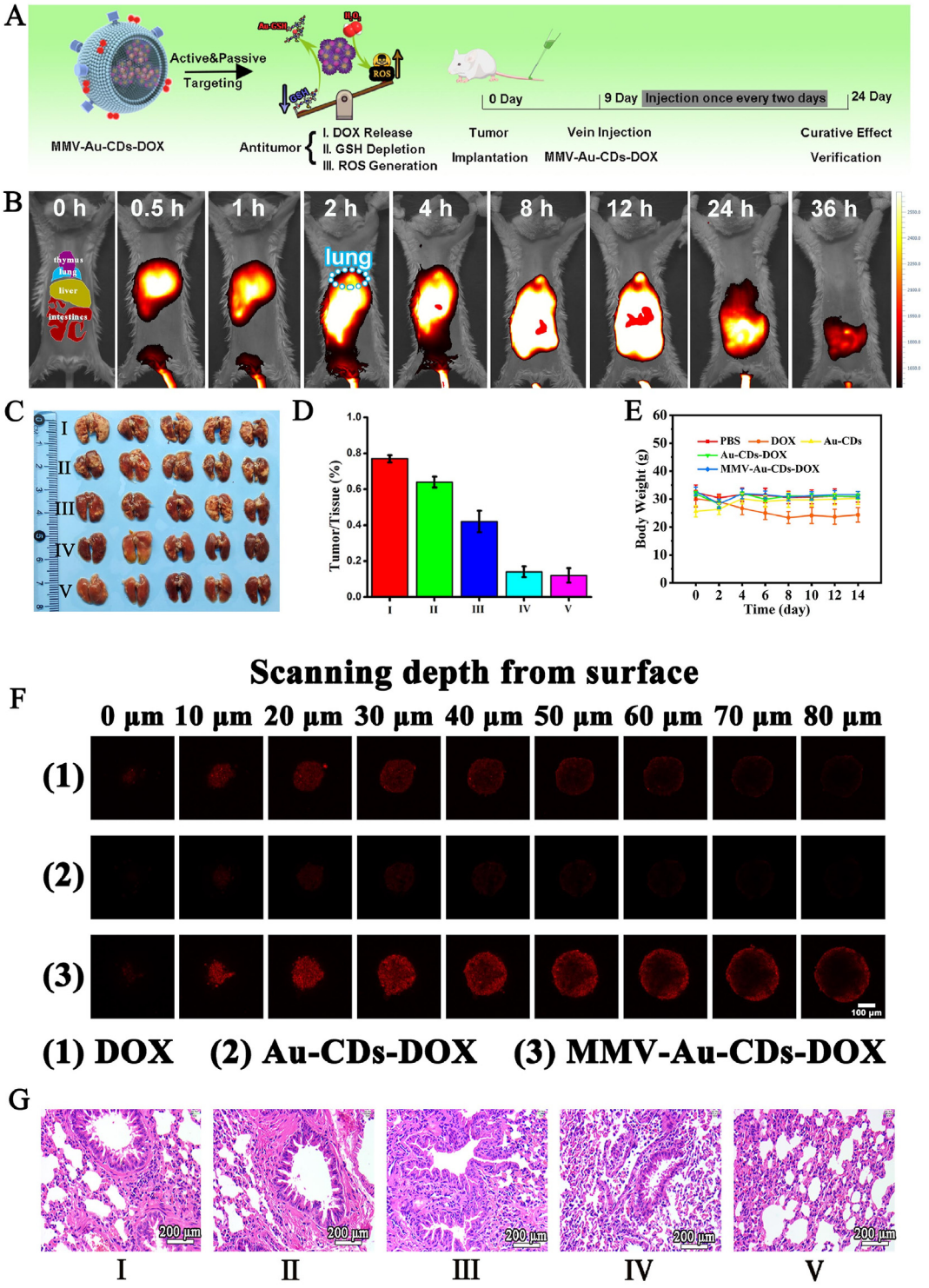

25

Fig. 6. *In vivo* anti-tumor activity of MMV-Au-CDs-DOX. (A) Schematic diagram of therapeutic mechanism and the specific treatment process of MMV-Au-CDs-DOX. (B) *In vivo* distribution of ICR mice with breast cancer lung metastasis treatment with MMV-Au-CDs-ICG. (C) Typical photographs of lungs from mice and (D) the quantitative analysis of tumor necrosis area after treated with saline alone (Group I), DOX alone (Group II), Au-CDs (Group III), Au-CDs-DOX (Group IV) and MMV-Au-CDs-DOX (Group V). (E) The weight changes of mice during the treatment for 15 days. (F) Tumor permeability verification of Au-CDs-DOX and MMV-Au-CDs-DOX via FIM images of 3D 4T1 tumor model. (G) Histological analysis of the lung lesion after treatment with different agents.

The drug release behaviors were further investigated. In the simulated TME condition (pH 5.0 or 7.4) with the addition of GSH, the release of DOX was ~71%, while only ~ 8% in the condition of natural plasma imitator (Fig. 4C). Cell uptake were further investigated by monitoring the fluorescence changes based on the PL signals of Au-CDs and DOX in real 4T1 cell (Fig. 5B). As well as the quantitative results of fluorescence of the intracellular DOX release was displayed in Fig. S13, manifesting that the green and red fluorescence intensity with MMV-Au-CDs-DOX treated both exceed that of Au-CDs-DOX group. Compared with Au-CDs, the distinctive green (Au-CDs) and red (DOX) fluorescence were simultaneously observed during Au-CDs-DOX and MMV-Au-CDs-DOX incubation with 4T1 cell for 4 h. Whereas, the additive intensity value of the different channels signals in MMV-Au-CDs-DOX was dramatically higher than cpc-CDs-AuNPs-DOX, which meant the MMV packaging might enhance cellular uptake.

For further confirming the antitumor activity and targeting, the cytotoxicity of different nano-drugs was tested from several aspects. First, MTT assay was used to evaluate (Fig. 5A). After being co-incubated with tumor (4T1) and normal (HUVEC) cells for 24 h, Au-CDs and Au-CDs-DOX exhibited similar trends as the survival rate of HUVEC was slightly lower than 4T1. However, the inhibitory effect of MMV-Au-CDs-DOX flipped due to the more uptake of 4T1, indicating clearly that the drug delivery system encapsulated by macrophage membranes could enhance the tumor targeting. Then, the cells are co-stained with the live/dead (calcein-AM/PI) dyes to visualize live (green fluorescence signal) and dead (red fluorescence signal) cells. As shown in Fig. S14, MMV-Au-CDs-DOX group manifested that a large percentage of dead cells are stained with red dyes and that of other treatments were far lower this the ratio. Moreover, as displayed in Fig. S15, the intracellular uptake level of MMV-Au-CDs-DOX was evaluated followed by the flow cytometry, which is accordance with the quantitative analysis of uptake. Results demonstrated that MMV-Au-CDs-DOX could perform excellent uptake, compared with other treatments.

3.5. *In vivo anti-tumor activity of MMV-Au-CDs-DOX nanocomposite*

Inspired by the above excellent tumor targeting and antitumor activity at the cellular level, the breast cancer lung metastasis model was further used to verify the relative therapeutic indexes *in vivo*. Herein, ICG, having the NIR fluorescence at ~805 nm and similar polarity to DOX, was chosen to replace DOX (the absorption and PL spectra were shown in Fig. S16) for trancing the nanocomposites *in vivo*, revealing the internal metabolism and distribution. MMV-Au-CDs-ICG (0.1 mg ICG/kg body weight) was injected intravenously into the pulmonary metastasis of 4T1 breast cancer in mice. The NIR small animal imaging system observed the PL signal of bio-distribution. As displayed in Fig. 6B, the signal of MMV-Au-CDs-ICG was found in tumor at 30 min after intravenous injection and extensively accumulated at tumor site over the next 2 h. Meanwhile, the main organs were collected at 2 h, and their fluorescence distribution were recorded (Fig. S17). The result showed that compared with Au-CDs-ICG administration, the fluorescence appeared in the lungs after MMV-Au-CDs-ICG treated for 2 h, manifesting that tumor-targeting effect of MMV-Au-CDs-DOX is ascribed to the existence of MMV.

Profiting by the favorable location targeting and the subsequent effective release of MMV-Au-CDs-ICG, we intentionally investigated MMV-Au-CDs-DOX feasibility and curative effect for treating ICR mice with breast cancer lung metastasis. Herein, mice were randomly divided into five groups (n = 5) receiving specific treatments with different remedies via tail vein, and the grouping was as follows: saline alone (Group I), DOX alone (Group II), Au-CDs (Group III), Au-CDs-DOX (Group IV) and MMV-Au-CDs-DOX (Group V). As shown in Fig. 6E, the mice weight of the positive DOX group gradually decreased during all the period of treatment, while the weight of negative control lost slightly relatively, which should be attributed to the intrinsic bio-toxicity of antitumor chemotherapeutic drugs for Group II, and might be the growth of tumors affected the food intake of mice and the excessive consumption of nutrients by the tumor tissues for Group I. Contrarily, the weight of mice in Group III to V did not change significantly, which seemed no apparent toxicity, and improve/even eliminate the side effects of DOX, indicating that transported by nano-vectors would be a beneficial delivery platform for therapeutic agents with some toxicity.

After two weeks of administration, the mice were sacrificed and separated the lungs ex vivo to observe the metastatic nodules. As shown in Fig. 6C–D, a large area of tumor necrosis tissue was found in the lungs of mice treated with saline, and slightly inhibition of lung metastasis was observed in mice treated with 5 mg/kg of DOX (~13% decrease compared with Group I), Au-CDs showed better inhibition of tumor growth than those of two former intervention groups. Remarkably, the metastatic nodules of mice decreased notably in Au-CDs-DOX and MMV-Au-CDs-DOX groups at an equivalent dose of 5 mg/kg (DOX/body weight). Although we did not focus on the therapeutic effect of Au-CDs alone on tumors, interestingly, Au-CDs present a better therapeutic efficacy compared with DOX, because Au NPs, besides as drug carrier, could also be labeled to target specific cancer cell ligands and therefore can be used to target only malignant cells, allowing Au NPs could be both theranostic and curative in nature [45]. Furthermore, from the results of sections of the lungs stained by H&E (Fig. 6G), tumor lesions were significantly reduced after Au-CDs-DOX and MMV-Au-CDs-DOX injection compared with these in negative, positive and materials control groups, indicating that Au-CDs could increase the drug accumulation at the tumor sites via EPR effect and inhibiting metastatic nodules. After biomimetic construction, the MMV-Au-CDs-DOX would inherit the superiority of Au-CDs and improve the active target to the lung metastasis site.

As the bio-toxicity, especially the strong cardiotoxicity, of free DOX, the toxicity to various organs was further investigated. The pathomorphology analysis of the main organs, including heart, liver, spleen, lung, and kidney was shown in Fig. S18. The heart section of the DOX treating mice exhibited significant lesion and lymphocytic invasion for the positive drug group, indicating high cardiotoxicity. By contrast, there were no apparent damages in the detected organs from other groups, implying that Au-CDs-DOX-based nanocomposites have good biocompatibility *in vivo*. In addition, the expression of the maker of liver (ALT, AST, ALP) and kidney (BUN, UR, CERA) when mice were administrated with the MMV-Au-CDs-DOX had no statistical difference, compared with PBS group (Fig. S19). 3D tumor spheroids model was used for further testing the tumor permeability of Au-CDs-DOX. As shown in Fig. 6F, the red fluorescence of DOX at the free DOX group was primarily observed on the outer layer of the tumor spheroids, nevertheless, the fluorescence diminished with scanning depth increased. While that at the MMV-Au-CDs-DOX group could be observed throughout the tumor spheroids, ascribed to the existence of MMV. Significantly, the intensity of fluorescence, for Au-CDs-DOX, is far lower than free DOX group, which could explain that the fluorescence of DOX was absorbed by Au-CDs due to FRET (Fluorescence Resonance Energy Transfer) phenomenon. In addition, ACQ (Aggregation-Caused Quenching) effect appeared when DOX was richly accumulated into tumor cells via Au-CDs carrier. These results indicated that Au-CDs could advance the permeability of DOX into tumor spheroids effectively causing by disintegrating into the smaller nanoparticles by the distinctive micro-environment of solid tumor.

4. Conclusion

In summary, a well-designed self-assembly Au-CDs, which exhibited GSH and H_2O_2 sensitive procedural disintegration and fluorescence enhancement was fabricated via “step by step” inter-particle assembled for tumor development stage detection and treatment. During the preparation, AuNPs was exploited as a mediation for in situ aggregation of cpc-CDs through Au–NH bonds, and the bonds could further completely dissociate when coexistence with sulfur compounds, which included the sensitivity tumor drug resistance detection for GSH and even the rational targeting drug release for oncotherapy. After artificially coated with macrophage-derived microvesicle, the obtained MMV-Au-CDs-DOX

would effectively target in tumor site, combing with the response disintegration of nanocomposites, higher curative effect and less side-effect was achieved. This study is interesting for exploiting a strategy to fabricate biocompatible CDs-based nanomaterials to improve the clinical applications of the combination of metal nanoparticles and carbon dots, and also provides an intriguing bio-application scenarios for the inorganic nanoparticles with similar structure.

Declaration of competing interest

The authors declare that they have no known competing financial interests or personal relationships that could have appeared to influence the work reported in this paper.

Acknowledgements

This work was financially supported by the China Postdoctoral Science Foundation (2019M653356), Chongqing Postdoctoral Science Foundation (cstc2019jcyjbshX0060), and the Introduction Teachers Foundation of Chongqing Medical University (YXY2018BSH1 and YXY2019BSH2).

Appendix A. Supplementary data

Supplementary data to this article can be found online at https://doi.org/10.1016/j.mtbio.2022.100359.

References

[1] J. Chen, Y. Zhu, C. Wu, J. Shi, Nanoplatform-based cascade engineering for cancer therapy, Chem. Soc. Rev. 49 (24) (2020) 9057–9094.
[2] Y. Dai, C. Xu, X. Sun, X. Chen, Nanoparticle design strategies for enhanced anticancer therapy by exploiting the tumour microenvironment, Chem. Soc. Rev. 46 (12) (2017) 3830–3852.
[3] P. Zhang, D. Gao, K. An, Q. Shen, C. Wang, Y. Zhang, et al., A programmable polymer library that enables the construction of stimuli-responsive nanocarriers containing logic gates, Nat. Chem. 12 (4) (2020) 381–390.
[4] H. Lin, Y. Chen, J. Shi, Nanoparticle-triggered in situ catalytic chemical reactions for tumour-specific therapy, Chem. Soc. Rev. 47 (6) (2018) 1938–1958.
[5] M. Zhang, X. Guo, M. Wang, K. Liu, Tumor microenvironment-induced structure changing drug/gene delivery system for overcoming delivery-associated challenges, J. Contr. Release 323 (2020) 203–224.
[6] L. Feng, B. Liu, R. Xie, D. Wang, C. Qian, W. Zhou, et al., An ultrasmall SnFe2O4 nanozyme with endogenous oxygen generation and glutathione depletion for synergistic cancer therapy, Adv. Funct. Mater. 31 (2020), 2006216.
[7] F. Gong, M. Chen, N. Yang, Z. Dong, L. Tian, Y. Hao, et al., Bimetallic oxide FeWOX nanosheets as multifunctional cascade bioreactors for tumor microenvironment-modulation and enhanced multimodal cancer therapy, Adv. Funct. Mater. 30 (49) (2020), 2002753.
[8] Q. Mao, J. Fang, A. Wang, Y. Zhang, C. Cui, S. Ye, et al., Aggregation of gold nanoparticles triggered by hydrogen peroxide-initiated chemiluminescence for activated tumor theranostics, Angew. Chem. Int. Ed. 60 (44) (2021) 23805–23811.
[9] K. Wang, J. Lu, J. Li, Y. Gao, Y. Mao, Q. Zhao, S. Wang, Current trends in smart mesoporous silica-based nanovehicles for photoactivated cancer therapy, J. Contr. Release 339 (2021) 445–472.
[10] S. Li, Y. Chen, W. Zhu, W. Yang, Z. Chen, J. Song, et al., Engineered nanoscale vanadium metallodrugs for robust tumor-specific imaging and therapy, Adv. Funct. Mater. 31 (17) (2021), 2010337.
[11] Z. Zhao, K. Xu, C. Fu, H. Liu, M. Lei, J. Bao, et al., Interfacial engineered gadolinium oxide nanoparticles for magnetic resonance imaging guided microenvironment-mediated synergetic chemodynamic/photothermal therapy, Biomaterials 219 (2019), 119379.
[12] T. Deng, J. Wang, Y. Li, Z. Han, Y. Peng, J. Zhang, et al., Carbon dots-based multifunctional nano-prodrug fabricated by ingenious self-assembly strategies for tumor theranostic, ACS Appl. Mater. Interfaces 10 (33) (2018) 27657–27668.
[13] E.E. Lees, T.L. Nguyen, A.H.A. Clayton, P. Mulvaney, B.W. Muir, The preparation of colloidally stable, water-soluble, biocompatible, semiconductor nanocrystals with a small hydrodynamic diameter, ACS Nano 3 (5) (2009) 1121–1128.
[14] L. Wang, W. Jiang, L. Xiao, H. Li, Z. Chen, Y. Liu, et al., Self-reporting and splitting nanopomegranates potentiate deep tissue cancer radiotherapy via elevated diffusion and transcytosis, ACS Nano 14 (7) (2020) 8459–8472.
[15] W. Xuan, Y. Xia, T. Li, L. Wang, Y. Liu, W. Tan, Molecular self-assembly of bioorthogonal aptamer-prodrug conjugate micelles for hydrogen peroxide and pH-independent cancer chemodynamic therapy, J. Am. Chem. Soc. 142 (2) (2020) 937–944.
[16] Z. Sheng, B. Guo, D. Hu, S. Xu, W. Wu, W.H. Liew, et al., Bright aggregation-induced-emission dots for targeted synergetic NIR-II fluorescence and NIR-I photoacoustic imaging of orthotopic brain tumors, Adv. Mater. 30 (2018), 1800766.
[17] H. Guo, Y. Zhang, W. Liang, F. Tai, Q. Dong, R. Zhang, et al., An inorganic magnetic fluorescent nanoprobe with favorable biocompatibility for dual-modality bioimaging and drug delivery, J. Inorg. Biochem. 192 (2019) 72–81.
[18] T. Wei, H. Xing, H. Wang, Y. Zhang, J. Wang, J. Shen, et al., Bovine serum albumin encapsulation of near infrared fluorescent nano-probe with low nonspecificity and cytotoxicity for imaging of HER2-positive breast cancer cells, Talanta 210 (2020), 120625.
[19] Q. Zhao, Y. Yang, H. Wang, W. Lei, Y. Liu, S. Wang, Gold nanoparticles modified hollow carbon system for dual-responsive release and chemo-photothermal synergistic therapy of tumor, J. Colloid Interface Sci. 554 (2019) 239–249.
[20] P. Gong, L. Sun, F. Wang, X. Liu, Z. Yan, M. Wang, et al., Highly fluorescent N-doped carbon dots with two-photon emission for ultrasensitive detection of tumor marker and visual monitor anticancer drug loading and delivery, Chem. Eng. J. 356 (2019) 994–1002.
[21] S. Feng, J. Lu, K. Wang, D. Di, Z. Shi, Q. Zhao, S. Wang, Advances in smart mesoporous carbon nanoplatforms for photothermal–enhanced synergistic cancer therapy, Chem. Eng. J. 435 (2022), 134886.
[22] J. Du, N. Xu, J. Fan, W. Sun, X. Peng, Carbon dots for in vivo bioimaging and theranostics, Small 15 (32) (2019), 1805087.
[23] Y.W. Bao, X.W. Hua, Y.H. Li, H.R. Jia, F.G. Wu, Hyperthermia-promoted cytosolic and nuclear delivery of copper/carbon carbon dot-crosslinked nanosheets: multimodal imaging-guided photothermal cancer therapy, ACS Appl. Mater. Interfaces 10 (2) (2018) 1544–1555.
[24] Y. Liu, X. Zhi, W. Hou, F. Xia, J. Zhang, L. Li, et al., Gd3+-Ion-induced carbon-dots self-assembly aggregates loaded with a photosensitizer for enhanced fluorescence/MRI dual imaging and antitumor therapy, Nanoscale 10 (40) (2018) 19052–19063.
[25] G. Aizik, N. Waiskopf, M. Agbaria, Y. Levi-Kalisman, U. Banin, G. Golomb, Delivery of liposomal carbon dots via monocytes for imaging of inflamed tissue, ACS Nano 11 (3) (2017) 3038–3051.
[26] J. Fu, L. Liang, L. Qiu, In situ generated gold nanoparticle hybrid polymersomes for water-soluble chemotherapeutics: inhibited leakage and pH-responsive intracellular release, Adv. Funct. Mater. 27 (18) (2017), 1604981.
[27] X. Cai, Z. Xie, B. Ding, S. Shao, S. Liang, M. Pang, et al., Monodispersed copper(I)-Based nano metal-organic framework as a biodegradable drug carrier with enhanced photodynamic therapy efficacy, Adv. Sci. 6 (15) (2019), 1900848.
[28] E. Ko, V.-K. Tran, S.E. Son, W. Hur, H. Choi, G.H. Seong, Characterization of Au@PtNP/GO nanozyme and its application to electrochemical microfluidic devices for quantification of hydrogen peroxide, Sensor Actuat. B-Chem. 294 (2019) 166–176.
[29] T. Deng, R. Zhang, J. Wang, X. Song, F. Bao, Y. Gu, et al., Carbon dots-cluster-DOX nanocomposites fabricated by a Co-Self-Assembly strategy for tumor-targeted bioimaging and therapy, Part. Part. Syst. Char. 35 (9) (2018), 1800190.
[30] C.Y. Han, X.M. Zhang, F. Wang, Q.H. Yu, F. Chen, D. Shen, et al., Duplex metal co-doped carbon carbon dots-based drug delivery system with intelligent adjustable size as adjuvant for synergistic cancer therapy, Carbon 183 (2021) 789–808.
[31] W. Ma, L. Xu, X. Li, S. Shen, M. Wu, Y. Bai, et al., Cysteine-functionalized metal-organic framework: facile synthesis and high efficient enrichment of N-linked glycopeptides in cell lysate, ACS Appl. Mater. Interfaces 9 (23) (2017) 19562–19568.
[32] G. Liu, E. Luais, J.J. Gooding, The fabrication of stable gold nanoparticle-modified interfaces for electrochemistry, Langmuir 27 (7) (2011) 4176–4183.
[33] E. Boisselier, D. Astruc, Gold nanoparticles in nanomedicine: preparations, imaging, diagnostics, therapies and toxicity, Chem. Soc. Rev. 38 (6) (2009) 1759–1782.
[34] Q.F. Zhao, Y. Yang, H.L. Wang, W. Lei, Y.X. Liu, S.L. Wang, Gold nanoparticles modified hollow carbon system for dual-responsive release and chemo-photothermal synergistic therapy of tumor, J. Colloid Interface Sci. 554 (2019) 239–249.
[35] X. Cheng, H.D. Xu, H.H. Ran, G. Liang, F.G. Wu, Glutathione-depleting nanomedicines for synergistic cancer therapy, ACS Nano 15 (5) (2021) 8039–8068.
[36] Y. Jiang, J. Cheng, C. Yang, Y. Hu, J. Li, Y. Han, et al., An ultrasensitive fluorogenic probe for revealing the role of glutathione in chemotherapy resistance, Chem. Sci. 8 (12) (2017) 8012–8018.
[37] R.A. Ward, S. Fawell, N. Floc'h, V. Flemington, D. Mckerrecher, P.D. Smith, Challenges and opportunities in cancer drug resistance, Chem. Rev. 121 (6) (2021) 3297–3351.
[38] Chenlu Wang, Hongxin Lin, Xiaoguang Ge, Jing Mu, Lichao Su, Xuan Zhang, Dye-sensitized downconversion nanoprobes with emission beyond 1500 nm for ratiometric visualization of cancer redox state, Adv. Funct. Mater. 16 (31) (2021), 2009942.
[39] Z. Li, J. Ni, L. Liu, L. Gu, Z. Wu, T. Li, et al., Imaging-guided chemo-photothermal polydopamine carbon dots for EpCAM-targeted delivery toward liver tumor, ACS Appl. Mater. Interfaces 13 (25) (2021) 29340–29348.
[40] Y.J. Chung, J. Kim, C.B. Park, Photonic carbon dots as an emerging nanoagent for biomedical and healthcare applications, ACS Nano 14 (6) (2020) 6470–6497.
[41] E. Galati, M. Tebbe, A. Querejeta-Fernandez, H.L. Xin, O. Gang, E.B. Zhulina, et al., Shape-specific patterning of polymer-functionalized nanoparticles, ACS Nano 11 (5) (2017) 4995–5002.

[42] Y. Ma, M. Zhang, P. Li, Z. Han, L. Wu, T. Li, et al., Multifunctional small molecule fluorophore for long-duration tumor-targeted monitoring and dual modal phototherapy, Part. Part. Syst. Char. 7 (34) (2017), 1700076.
[43] C. Chen, M. Song, Y. Du, Y. Yu, C. Li, Y. Han, et al., Tumor-associated-macrophage-membrane-coated nanoparticles for improved photodynamic immunotherapy, Nano Lett. 21 (13) (2021) 5522–5531.
[44] R. Li, Y. He, Y. Zhu, L. Jiang, S. Zhang, J. Qin, et al., Route to rheumatoid arthritis by macrophage-derived microvesicle-coated nanoparticles, Nano Lett. 19 (1) (2019) 124–134.
[45] D.M. Connor, A.M. Broome, Gold nanoparticles for the delivery of cancer therapeutics, Adv. Cancer Res. 139 (2018) 163–184.